




Effect of g-C₃N₄ on structural, optical, and photocatalytic properties of hexagonal cylinder-like twinned ZnO microcrystals prepared by the hydrothermal method

T. P. Vijayakumar^{1,*} , M. D. Benoy², J. Duraimurugan³, G. Suresh Kumar⁴, S. Shanavas⁵, P. Maadeswaran^{6,7}, and Roberto Acevedo⁸

¹Research and Development Centre, Bharathiar University, Coimbatore, Tamil Nadu 641046, India

²Department of Physics, Mar Athanasius College (Autonomous), Kothamangalam, Kerala 686666, India

³Department of Physics, Laxminarayana Arts and Science College for Women, Dharmapuri, Tamil Nadu 636705, India

⁴Department of Physics, K.S. Rangasamy College of Arts and Science (Autonomous), Tiruchengode, Tamil Nadu 637215, India

⁵Department of Physics, Periyar University, Salem, Tamil Nadu 636011, India

⁶Department of Energy Science, Periyar University, Salem, Tamil Nadu 636011, India

⁷Center for Instrumentation and Maintenance Facility, Periyar University, Salem, Tamil Nadu 636011, India

⁸Facultad de Ingeniería y Tecnología, Universidad San Sebastián, Bellavista 7, 8420524 Santiago, Chile

Received: 12 May 2021

Accepted: 18 August 2021

Published online:

4 September 2021

© The Author(s), under exclusive licence to Springer Science+Business Media, LLC, part of Springer Nature 2021

ABSTRACT

The effect of g-C₃N₄ on the structural, optical, and photocatalytic properties of ZnO microcrystals under hydrothermal conditions was investigated in this research. The addition of g-C₃N₄ changed not only the phase composition, but also affect the growth of ZnO crystals, changing the lattice parameter and the transformation of hexagonal cylinder-like twinned ZnO microcrystals (1–2 μm length and 0.5–1 μm diameter) to g-C₃N₄ amalgamated rice-like ZnO nanostructure (500 nm length and 100 diameter) with type II heterojunction. The optical bandgap was found to be 3.27 and 3.21 eV for pristine ZnO and g-C₃N₄@ZnO, respectively. Owing to the narrow bandgap (2.7 eV) of g-C₃N₄, a red shift towards the visible region in optical absorption and a substantial reduction in the optical bandgap was observed for g-C₃N₄@ZnO heterostructure. Besides, it is also found that g-C₃N₄@ZnO has significantly higher photocatalytic effect (93 %) on RhB dye degradation than pristine ZnO (70 %) and g-C₃N₄ (68 %), because it produce a large number of reactive species (·OH and O₂^{•-} radicals) by hold-up the recombination of charge carriers via type II heterojunction. This research may be one of the most realistic approaches to developing effective photocatalysts for environmental remediation.

Address correspondence to E-mail: tpvkumarmscbed@gmail.com

1 Introduction

Toxic colorants in wastewater discharged from textile mills are the main source of water and soil contamination. To minimize environmental pollution, a range of methods for removing toxic colorants from textile wastewater have been developed [1, 2]. Physical, chemical, biological, and hybrid approaches are among them. The most commonly used harmful dye in the textile industry is Rhodamine B (RhB) [3, 4]. Researchers have focused their attention on the removal of RhB dye from textile wastewater via chemical processes particularly using a photocatalyst because it can turn the dye molecules into carbon dioxide, water, and mineral acids without generating secondary pollutants [4]. Because of low cost, and high photochemical reactivity, metal oxides have emerged as the leading photocatalyst for dye degradation in recent years [5].

Among different metal oxides, zinc oxide (ZnO) is a well-known II–VI compound semiconductor metal oxide due to its attractive physical and chemical properties [6–8]. Owing to fascinating inherent characteristics, ZnO is widely applied for making photocatalysts, LED, gas sensors, ultraviolet lasers, photodetectors, solar cells, and so on [6–8]. The energy band gap, micro/nanostructure, defects, and composition of the ZnO played an essential role in the above-said applications [6–10]. In recent decades, it has become possible to manipulate the micro/nanostructure of ZnO by novel chemical and physical processes for bandgap engineering [8, 9]. As a result, scientists have evolved various processing methods such as co-precipitation, sol-gel, hydrothermal, microwave, and microemulsion to obtain ZnO micro/nanostructure with tunable physical and chemical properties [8, 10, 11]. One of the most popular and unique methods for preparing ZnO is hydrothermal synthesis because it offers ZnO with high crystallinity, good purity, well dispersibility, controlled particle size, and morphology [10, 12–14]. Several researchers have also used metal ion doping and making composites to engineer the bandgap of ZnO through hydrothermal synthesis for photocatalytic applications [13, 14].

On the other hand, graphitic carbon nitride ($g\text{-C}_3\text{N}_4$), an excellent material, has attracted widespread interest as a visible light sensitive photocatalyst for dye degradation owing to high chemical

stability, and small bandgap (~ 2.7 eV) [15, 16]. However, its usage in environmental remediation is limited because of poor quantum performance, ultrafast electron-hole (e–h) pair recombination, and low surface area [16]. Based on the literature review, one of the most practical ways to obtain a better photocatalyst is fabricating heterostructures [17–20]. The interface between two distinct semiconductors with uneven band structures is known as a heterojunction. The heterostructured photocatalysts are classified into three types based on their band alignment: type-I (straddling gap), type-II (staggered gap), type-III (broken gap) [21]. The $g\text{-C}_3\text{N}_4/\text{ZnO}$ heterostructure belongs to a type-II heterojunction photocatalyst in which the conduction band (CB) and valence band (VB) of $g\text{-C}_3\text{N}_4$ semiconductor are greater than the respective levels of ZnO semiconductor. Thereby, under light irradiation, the photo-generated e^- can migrate into ZnO and the photo-generated h^+ can migrate into $g\text{-C}_3\text{N}_4$, leading to a complete separation of charge carriers which is constructive for photocatalytic degradation of organic dyes. Le et al. prepared ZnO/ $g\text{-C}_3\text{N}_4$ nanocomposites *via* the hard-templating method for the effective photocatalytic degradation of methyl orange [17]. Yang et al. applied a hydrothermal approach to creating a mesoporous $g\text{-C}_3\text{N}_4/\text{ZnO}$ photocatalyst for improved photocatalytic degradation of MB dye under visible light [18]. Qamar et al. used a co-precipitation process with PVP as a capping agent to construct highly effective $g\text{-C}_3\text{N}_4/\text{Cr-ZnO}$ nanocomposite for photocatalytic degradation of MB dye [19]. Manimozhi et al. synthesized $g\text{-C}_3\text{N}_4/\text{ZnO}$ heterostructure photocatalyst by hydrothermal method for enhanced visible degradation of crystal violet dye [20].

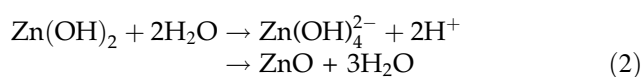
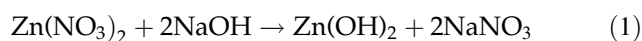
The photocatalytic reactions occur at the solid-solution interface hence numerous studies were carried out, including the study of the effect of crystal structure, to improve catalytic activity and to fulfill the demands for novel materials under visible region [22–24]. Nishikawa et al. found that the lattice distortion in the crystal structure of titanium oxide can enhance photocatalytic performance by promoting the effective separation of the charge carriers [22]. Basal et al. found that the monoclinic ZrO_2 has a higher methyl orange degrading activity than the tetragonal or cubic ZrO_2 phase [23]. Boppella et al. investigated the morphology-dependent enhanced photocatalytic degradation of MB dye under UV-light

and demonstrate the facet-dependent photocatalytic activity in ZnO crystals [24]. In this study, we investigate the effect of g-C₃N₄ on structural, morphological, optical, and photocatalytic characteristics of the hexagonal cylinder-like twinned ZnO microcrystals to obtain the photocatalyst with enhanced the light-harvesting abilities, reduced recombination of electron-hole pairs, and enhanced surface active sites for the photocatalytic degradation of RhB dye towards environmental remediation.

2 Materials and methods

2.1 Synthesis procedure

Merck, India, offered compounds such as sodium hydroxide (NaOH), urea (CH₄N₂O), and zinc nitrate (Zn(NO₃)₂), which were used for synthesis with no further cleaning. The solvent used was double-distilled water. The g-C₃N₄ was prepared *via* thermal combustion of dried urea (5 g) at 570 °C for 3 h in a muffle furnace [15, 25]. The resultant pale-yellow combusted substance was milled and preserved for subsequent use. The hydrothermal method was used to produce pristine ZnO and g-C₃N₄@ZnO. To synthesize pristine ZnO, 0.1 M Zn(NO₃)₂ was dissolved in 100 ml double-distilled water under continuous stirring, and then 0.2 M NaOH solution was introduced to bring the pH of the precursor solution to 13. After 1 h mixing, the collected resulting mixture was hydrothermally treated for 14 h at 130 °C. After the hydrothermal treatment, the collected precipitation was subjected to centrifugation at 5000 rpm to eliminate the waste products. The acquired precipitate was further dehydrated at 150 °C for 8 h to obtain the end product (pristine ZnO) according to the reaction (1) and (2) [10, 11].



To know the effect of g-C₃N₄ on the formation of ZnO, 5wt.% g-C₃N₄ was added with 100 mL of 0.1 M Zn(NO₃)₂ solution while stirring continuously. Then, the pH of the mixture was adjusted to 13 with the aid of 0.2 M NaOH solution. After 1 h mixing, the obtained resulting mixture was put into an autoclave at 130 °C for 14 h. After the hydrothermal treatment,

the obtained precipitation was centrifuged at 5000 rpm to take out the by-products. The acquired precipitate was further dried out at 150 °C for 8 h to obtain the final product and was named as g-C₃N₄@ZnO.

2.2 Characterization

The X-ray diffraction (XRD) patterns of pristine ZnO and g-C₃N₄@ZnO samples were recorded in the 10°–80° 2θ range using Cu Kα source (1.5406 Å) on a X-ray diffractometer (SHIMADZU LabX XRD-6100, Shimadzu Corporation, Japan) at 10°/min scan speed in the continuous mode. Using a Fourier-transform infrared (FTIR) spectrometer (RX1, Perkin Elmer Inc., USA), the FTIR spectrum of the sample was recorded in the 4000–400 cm⁻¹ range with the aid of the KBr pellet technique. The morphological characteristics were examined using a scanning electron microscope (SEM, ZEISS Ultra plus, Germany) and a high-resolution transmission electron microscope (HRTEM, JEM 2100, JEOL Ltd., Japan). Ultraviolet-visible diffuse reflectance spectrum (DRS) was recorded in the 200–800 nm wavelength range with 0.1 nm resolution using a UV-Vis-NIR spectrophotometer (Varian, Cary 5000) with DRS mode. X-ray photoelectron spectrum (XPS) was obtained using a XPS spectroscope (Multilab 2000, Thermo Scientific Instruments, USA) equipped with a twin anode Mg/Al (300/400 W) X-ray source.

2.3 Photocatalytic activity study

Under visible light, the photocatalytic degradation of RhB dye in the presence of pristine ZnO and g-C₃N₄@ZnO was examined under a halogen lamp (500 W, λ = 350–950 nm), 100 mL aqueous RhB solution (50 mg/L) was treated with 100 mg of prepared photocatalyst for 150 min. Subsequently, a sufficient volume of the supernatant RhB solution was taken at various intervals via centrifugation to determine the degradation of RhB molecules with the aid of a UV-visible Spectrophotometer (UV-1800, Shimadzu Corporation, Japan). The photocatalytic degradation efficiency of the photocatalyst was determined using the relation (3) [26].

$$\begin{aligned} \text{Photocatalytic degradation efficiency } \eta \\ = \left(1 - \frac{C_t}{C_0}\right) \times 100 \end{aligned} \quad (3)$$

where C_0 and C_t represent the concentration of RhB dye solution before and after treatment at an appropriate time (t).

2.4 Electrochemical analysis

The Mott–Schottky test was done through the electrochemical analysis using a computer-aided three-electrode apparatus under dark conditions at potential + 0.4 V. The sample coated electrode, Ag/AgCl electrode, and platinum wire was used as the working, reference, and counter electrode respectively. The Mott–Schottky plot was used to analyze the electronic band edges of the catalysts.

3 Results and discussion

3.1 XRD analysis

The recorded XRD pattern for the pristine ZnO and $g\text{-C}_3\text{N}_4@ZnO$ samples is shown in Fig. 1. The diffraction from planes was compared to a typical JCPDS pattern of zinc oxide (JCPDS file no. 89-1397). The pristine ZnO showed diffraction at 31.7° , 34.3° , 36.2° , 47.3° , 56.5° , 62.8° , 66.4° , 68.0° , 69.1° , 72.4° , and 76.9° corresponding to (002), (100), (101), (102), (110), (103), (200), (112), (201), (004), and (202) Miller's planes which are ascribed to hexagonal wurtzite structured ZnO phase. No further diffraction peaks were detected for pristine ZnO. However, the $g\text{-C}_3\text{N}_4@ZnO$ sample had typical ZnO diffraction peaks, as well as an extra diffraction peak at 27.2°

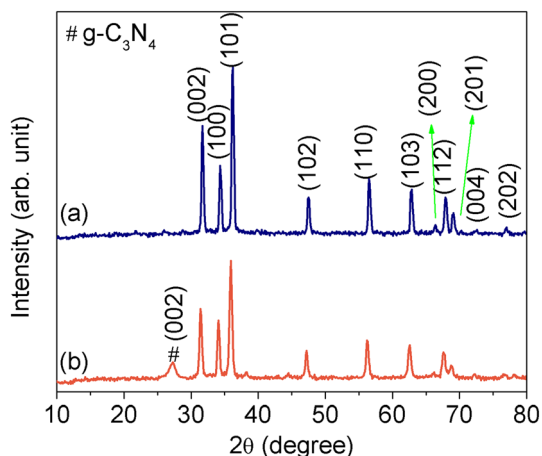


Fig. 1 The typical XRD pattern for (a) pristine ZnO and (b) $g\text{-C}_3\text{N}_4@ZnO$ samples

corresponding to (002) Miller's planes, (JCPDS file no. 87-1526), indicating the presence of both $g\text{-C}_3\text{N}_4$ and ZnO crystalline phases.

In comparison to $g\text{-C}_3\text{N}_4@ZnO$, pristine ZnO has sharper diffraction peaks, indicating that it has a high crystalline content. The lattice constants (a and c) of the hexagonal wurtzite structure were determined through the relation (4) [27].

$$\frac{1}{d^2} = \frac{4(h^2 + hk + k^2)}{3a^2} + \frac{l^2}{c^2} \quad (4)$$

where d denoted the lattice spacing, which was calculated using the relation $2d\sin\theta = n\lambda$ (Bragg's formula). Further, the unit cell volume of hexagonal wurtzite structure was calculated using the relation $V = 0.866 a^2c$ [27]. Table 1 shows the measured lattice constants and volume of the hexagonal unit cell for zinc oxide and it is well correlated with published results [11, 26]. Between ZnO and $g\text{-C}_3\text{N}_4@ZnO$, there was a substantial variation in the lattice constants and volume of the hexagonal unit cell of zinc oxide. In addition, compared to $g\text{-C}_3\text{N}_4@ZnO$, pristine ZnO had a reduced amount of lattice distortion (c/a). These findings revealed that $g\text{-C}_3\text{N}_4$ not only affect the phase composition but also has a major impact on the growth of ZnO crystals by interacting with zinc precursor during the formation.

3.2 Morphological analysis

Figure 2 shows the morphological characteristics of ZnO observed through SEM and TEM at different magnifications which revealed the hexagonal cylinder-like twinning microstructure with 1–2 μm length and 0.5–1 μm breadth. Figure 2d shows the precise hexagonal face of the microcrystals. The formation of the hexagonal cylinder-like ZnO microcrystal with twinned structure at hydrothermal condition is explained as follows: When zinc precursor is added

Table 1 Calculated lattice parameters for the pristine ZnO and $g\text{-C}_3\text{N}_4@ZnO$ samples

Sample code	Lattice parameters			
	$a = b$ (Å)	c (Å)	V (Å ³)	c/a
Pristine ZnO	3.1878	5.5276	48.64	1.7339
$g\text{-C}_3\text{N}_4@ZnO$	3.2057	5.5671	49.54	1.7366

with NaOH at alkaline condition, zinc ions can easily interact with hydroxyl ions and form Zn(OH)_2 . Subsequently, Zn(OH)_4^{2-} reactive species are formed *via* the reaction between Zn(OH)_2 and OH ions. At hydrothermal conditions, Zn(OH)_4^{2-} reactive species decomposed into ZnO nuclei, and further growth can be attributed to the growth habit of ZnO [10, 11].

It is well known that zinc (or oxygen) atoms are tetrahedrally attached with four oxygen (or zinc or) atoms and crystallize in a wurtzite-type structure with hexagonal symmetry [6, 7]. Hence, the further growth of ZnO units leads to hexagonal cylinder structure owing to its favorable growth habit along the *c*-axis i.e., hexagonal symmetry [10, 11]. Finally, the formed two hexagonal cylinder-like microcrystals can interact with each other along the *c*-axis due to the Coulomb interaction and form a hexagonal cylinder-like twinning microstructure as shown in Fig. 2c.

Figure 3 shows the morphological characteristics of $\text{g-C}_3\text{N}_4@\text{ZnO}$ observed through SEM and TEM at different magnifications which show that the rice-like ZnO nanocrystals were amalgamated with the $\text{g-C}_3\text{N}_4$ matrix. The length and breadth of rice-like ZnO nanocrystals were found to be 500 nm and 100 nm, respectively. Further, this observation revealed the superior interfacial contact of $\text{g-C}_3\text{N}_4@\text{ZnO}$ and the formation of $\text{g-C}_3\text{N}_4@\text{ZnO}$ heterostructure. When

$\text{g-C}_3\text{N}_4$ was introduced during the formation of Zn(OH)_4^{2-} reactive species from zinc precursor, the growth of ZnO nuclei was hindered by $\text{g-C}_3\text{N}_4$ species that formulate the growth habit and form $\text{g-C}_3\text{N}_4$ amalgamated rice-like ZnO heterostructure at the nanoscale. Comparison of Figs. 2 and 3 shows that the typical hexagonal cylinder-like twinning ZnO microstructure can be manipulated into rice-like ZnO heterostructure by the addition of $\text{g-C}_3\text{N}_4$ during the formation at hydrothermal conditions.

3.3 XPS analysis

The oxidation state of the prepared $\text{g-C}_3\text{N}_4@\text{ZnO}$ heterostructure was investigated using X-ray photoelectron spectroscopy which is shown in Fig. 4. The existence of Zn, O, C and Ni were revealed from the wide scan spectrum of $\text{g-C}_3\text{N}_4@\text{ZnO}$ heterostructure (Fig. 4a). Figure 4b shows peaks at 1022.08 eV and 1045.08 eV which are consistent with the binding energy of Zn^{2+} in the wurtzite structure of ZnO [28–30]. The high-resolution spectrum of O1s in Fig. 4c shows a peak at binding energy value of 531.08 eV which is ascribed to O^{2-} ions surrounded by Zn atom in the wurtzite structure [24–26]. The high-resolution spectrum of C1s in Fig. 4d has two peaks at binding energy values of 285.08 eV and 288.08 eV which are ascribed to adventitious carbon

Fig. 2 a & b SEM and c & d TEM images of pristine ZnO sample at different magnifications

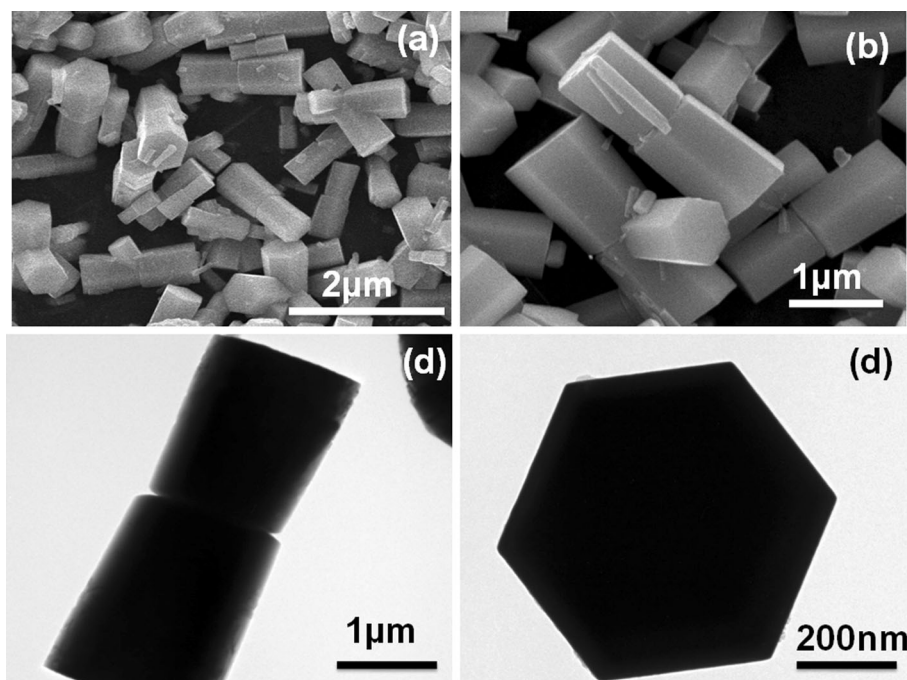
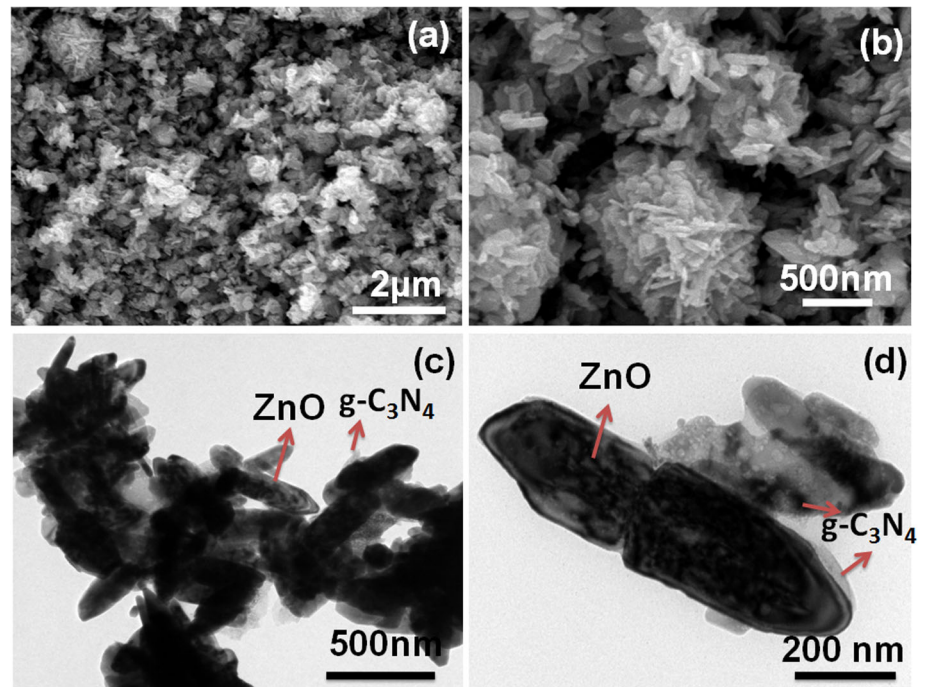


Fig. 3 a & b SEM and c & d TEM images of pristine g-C₃N₄@ZnO sample at different magnifications



C–C and sp²-hybridized carbon in the aromatic structure (N–C = N), respectively [28, 29]. N1s spectrum at high resolution in Fig. 4e shows a peak at 400.08 eV depicted tertiary N atoms (N–C3) [29]. The obtained binding energy value of Zn, O, C, and N clearly shows the formation of g-C₃N₄@ZnO heterostructure which could be effective in increasing the photocatalytic behavior by enhancing charge carrier transfer.

3.4 Optical Properties

The optical characteristics of the prepared pristine ZnO and g-C₃N₄@ZnO were studied through UV-vis DRS which is revealed in Fig. 5a. Pristine ZnO shows a sharp absorption edge at 373 nm while a redshift toward the visible region was observed for g-C₃N₄@ZnO as pure g-C₃N₄ has an absorption edge at 440 nm [31]. The optical bandgap for the prepared sample was calculated using reflectance value *via* a Tauc plot, i.e., the relation between optical absorption coefficient and incident photon energy. The relation between incident photon energy, optical absorption coefficient (α), and optical band gap (E_g) of the semiconductor is described by the relation (5) [32–34].

$$\alpha h\nu = A(h\nu - E_g)^n \quad (5)$$

where ν denotes the frequency of incident light, h and A are Planck's and proportionality constants, respectively and n represents the typical optical transition of semiconducting materials which is equal to 1/2 for zinc oxide. As a result, the relation (4) can be obtained [28–30].

Thereafter, the optical bandgap for the prepared samples was calculated by plotting $h\nu$ vs. $(\alpha h\nu)^2$ which is shown in Fig. 5b. The optical band gap was found to be 3.27 and 3.21 eV for pristine ZnO and g-C₃N₄-ZnO, respectively. A significant reduction in the optical bandgap for g-C₃N₄@ZnO was observed which could be attributed to the presence of the g-C₃N₄ component. The optical bandgap of g-C₃N₄ was estimated using a Tauc plot from UV-vis reflectance spectrum (Fig. S1 and S2) (supplementary material) which is low compared with ZnO. It can lead to possible fluctuations in the electronic band structure of g-C₃N₄@ZnO heterostructure resulted in a significant reduction in bandgap energy value [17–20]. The optical properties are a key factor to determine the photocatalytic activity of semiconductors hence the observed reduction in bandgap energy value should be substantial for further application.

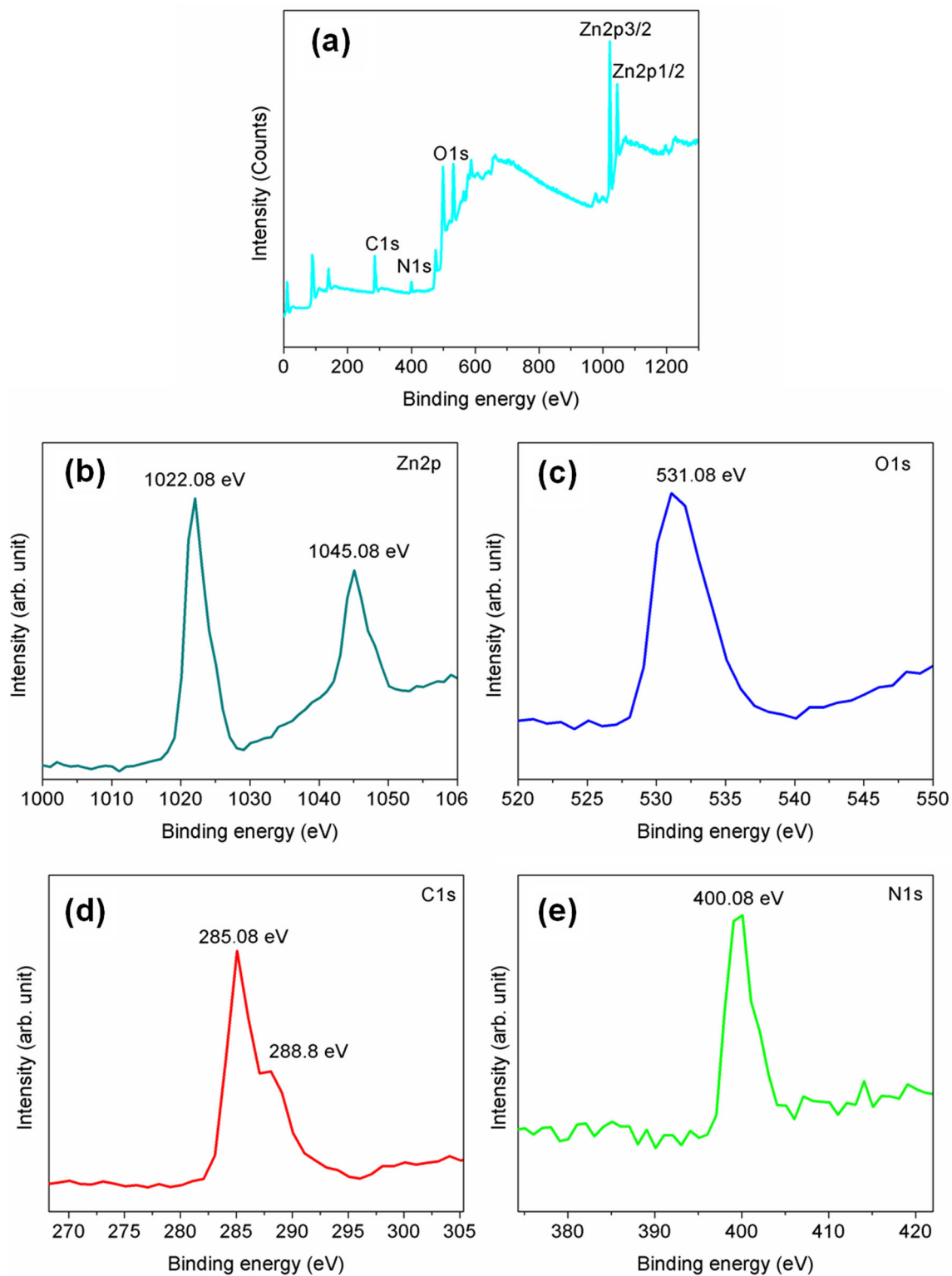


Fig. 4 X-ray photoelectron spectra of the $g\text{-C}_3\text{N}_4@\text{ZnO}$ photocatalyst **a** survey spectrum, **b–e** high-resolution spectrum of Zn2p, O1s, C1s and N1s

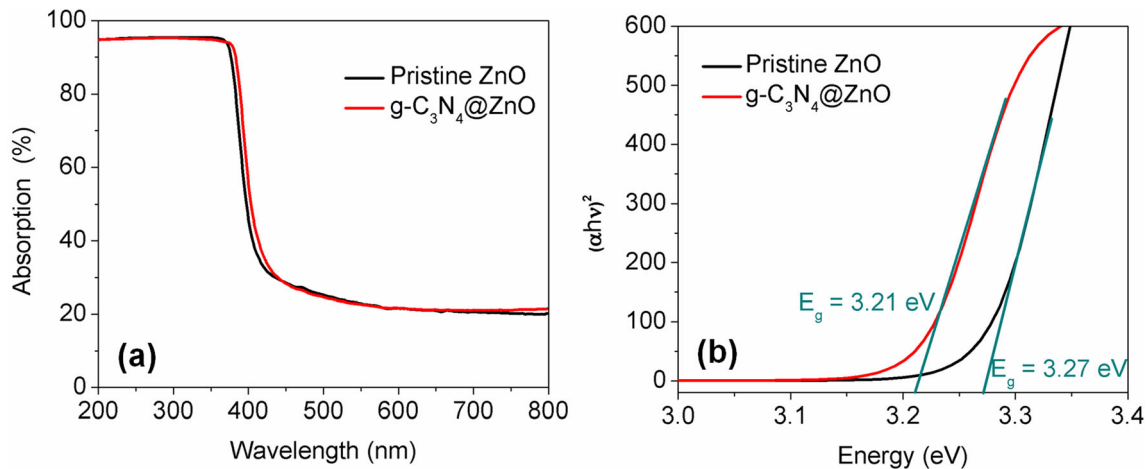


Fig. 5 **a** UV-Vis reflectance spectrum and **b** Tauc plot of prepared pristine ZnO and $g\text{-C}_3\text{N}_4@\text{ZnO}$ photocatalyst

3.5 Mott–Schottky plot analysis

The Mott-Schottky plot for pure ZnO and $g\text{-C}_3\text{N}_4$ are shown in Fig. 6. It revealed the positive slop which confirming that the prepared $g\text{-C}_3\text{N}_4$ and ZnO are n-type semiconductors. The flat band potential (E_{fb}) of ZnO and $g\text{-C}_3\text{N}_4$ were found to be -0.2 and -1.12 eV, respectively. The conduction band (CB) edge was situated close to the E_{fb} for n-type semiconductor, hence the obtained values were considered as CB edge of the prepared ZnO and $g\text{-C}_3\text{N}_4$. Using these values, the valence band (VB) of ZnO and $g\text{-C}_3\text{N}_4$ was calculated via relation (6) as $+3.2$ and $+1.57$ eV vs. NHE.

$$E_{VB} = E_{CB} + E_g \quad (6)$$

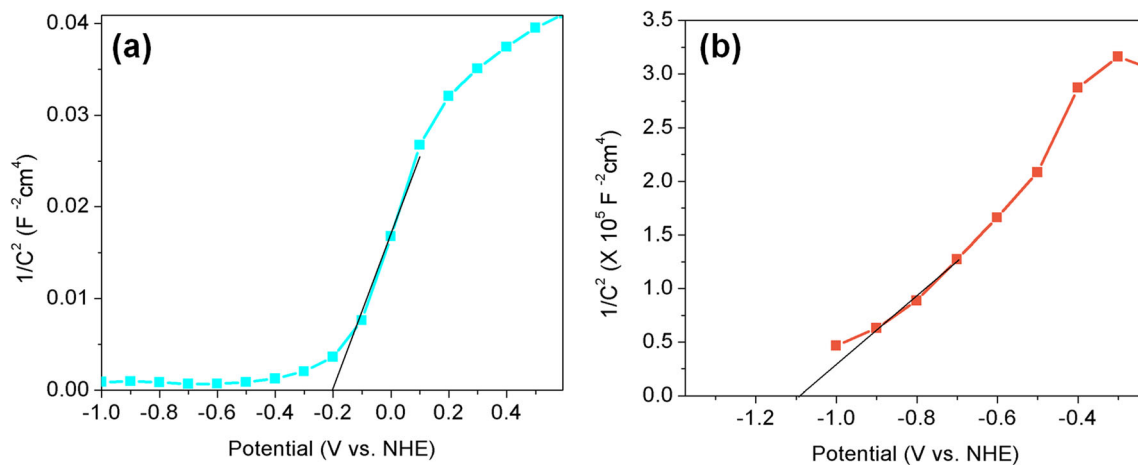


Fig. 6 The Mott–Schottky plot for **a** pure ZnO and **b** $g\text{-C}_3\text{N}_4$ samples

As a result, the band structure can be estimated which is thermodynamically suitable for photocatalytic degradation of RhB.

3.6 Photocatalytic performance

The photocatalytic oxidation of RhB in the presence of the prepared pristine ZnO and $g\text{-C}_3\text{N}_4@\text{ZnO}$ samples is included in this analysis to assess their photocatalytic function. UV-vis absorption spectra of RhB aqueous solution after varying periods of light irradiation in the presence of pristine ZnO and $g\text{-C}_3\text{N}_4@\text{ZnO}$ samples as the photocatalyst are shown in Fig. 7 a and b. Also, the time-dependent UV-Vis absorption spectrum of RhB aqueous solution for pure $g\text{-C}_3\text{N}_4$ is shown in Fig. S3 (supplementary material). It is found that the magnitude of the maximum absorption (λ_{max}) at 553 nm decreases

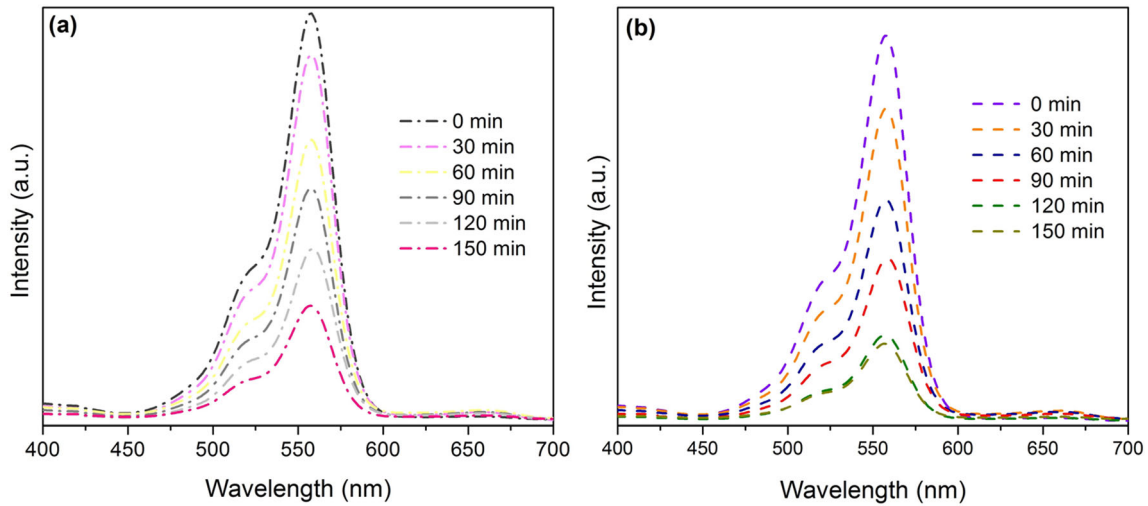


Fig. 7 UV–Vis absorption spectra of RhB aqueous solution after light irradiation at different periods. **a** pristine ZnO and **b** $g\text{-C}_3\text{N}_4@\text{ZnO}$ photocatalyst

rapidly with time, implying that pristine ZnO and $g\text{-C}_3\text{N}_4@\text{ZnO}$ samples can effectively oxidize the RhB dye when exposed to light than pure $g\text{-C}_3\text{N}_4$. The dye degradation efficiency versus reaction time graph for pristine ZnO and $g\text{-C}_3\text{N}_4@\text{ZnO}$ samples was obtained based on λ_{max} , as shown in Fig. 8. $g\text{-C}_3\text{N}_4@\text{ZnO}$ has a significantly higher photocatalytic activity than pristine ZnO. After 150 min of light irradiation, the photodegradation efficiency was found to be 70 and 93 % for pristine ZnO and $g\text{-C}_3\text{N}_4@\text{ZnO}$, respectively. The dye degradation efficiency of pure $g\text{-C}_3\text{N}_4$ was found to be 68 % (supplementary material Fig. S4) which is less than that of pristine ZnO and $g\text{-C}_3\text{N}_4@\text{ZnO}$ samples.

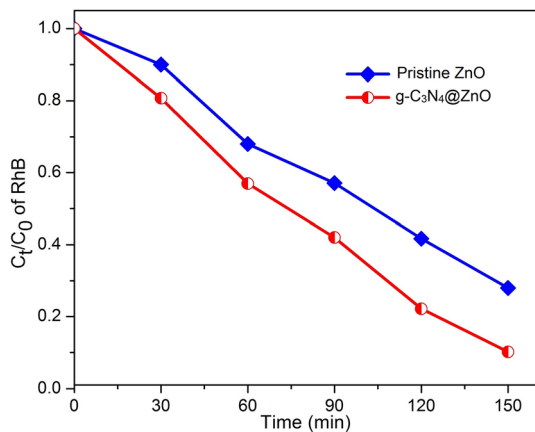


Fig. 8 The degradation ratio of RhB after light irradiation at different periods in the presence of pristine ZnO and $g\text{-C}_3\text{N}_4@\text{ZnO}$ photocatalyst

To know the kinetics of RhB dye degradation, the degradation ratio was fitted with the first-order kinetics according to relation (7) [35]

$$\ln\left(\frac{C_t}{C_0}\right) = kt \tag{7}$$

where k is the rate constant. Figure 9 shows the relation between the degradation ratio of RhB and time which shows a linear relation with $R^2 = 0.8873$ and $R^2 = 0.9165$ for pristine ZnO and $g\text{-C}_3\text{N}_4@\text{ZnO}$, respectively. This result shows that RhB dye degradation in the presence of both photocatalysts follows first-order kinetics. It is mentioned that the RhB degradation rate by pure $g\text{-C}_3\text{N}_4$ was also followed first-order kinetics according to Fig. S5

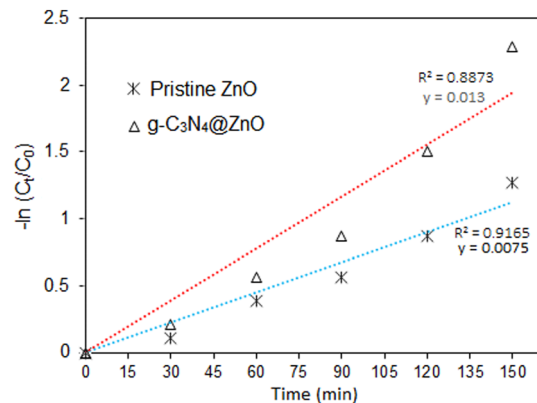


Fig. 9 Degradation kinetics of RhB after light irradiation at different periods in the presence of pristine ZnO and $g\text{-C}_3\text{N}_4@\text{ZnO}$ photocatalyst

(supplementary material). The reusability of prepared $g\text{-C}_3\text{N}_4@\text{ZnO}$ was also investigated (supplementary material Fig. S6), revealed that it can degrade RhB dye up to successive five cycles without significant variation.

The predominant active species involved during the photocatalytic dye degradation process was identified using a trapping experiment. In the trapping experiment, active species trapping chemical is added in the typical photocatalytic dye degradation experiment discussed above to suppress the generation of specific active species. During the trapping experiment, triethanolamine (TEOA), isopropyl alcohol (IPA), and benzoquinone (BQ) are used as a suppressor of h^+ , $\cdot\text{OH}$, and $\text{O}_2^{\bullet-}$ radicals, respectively. The trapping experiment clearly shows that the photocatalytic degradation efficiency is affected hugely after the addition of BQ and IPA with the degradation efficiency of about 25 and 40 %, respectively (Fig. 10). While after the addition of TEOA the photocatalytic degradation efficiency was found to be 80 %. The obtained results clearly (Fig. 10) show that the $\text{O}_2^{\bullet-}$ is the predominant reactive species involved during the photocatalytic dye degradation process followed by the $\cdot\text{OH}$ radicals.

Based on Tauc and Mott–Schottky plots, the energy band structure was obtained (Fig. 11) which revealed the possibility of formation of type (II) heterostructure in the prepared $g\text{-C}_3\text{N}_4@\text{ZnO}$ sample which can easily produce sufficient $\cdot\text{OH}$ and $\text{O}_2^{\bullet-}$ radicals for the photocatalytic dye degradation than the pure one.

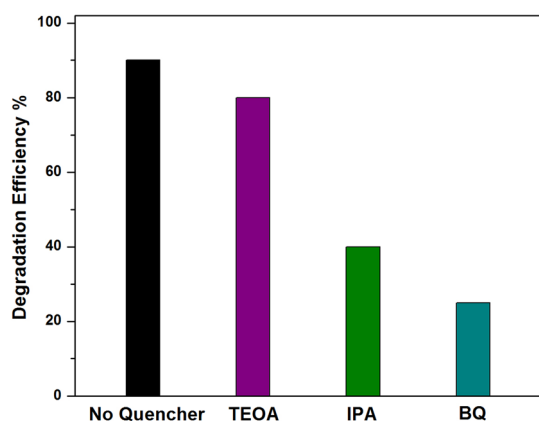


Fig. 10 The trapping experiment represents the predominant active species involved during the photocatalytic dye degradation process

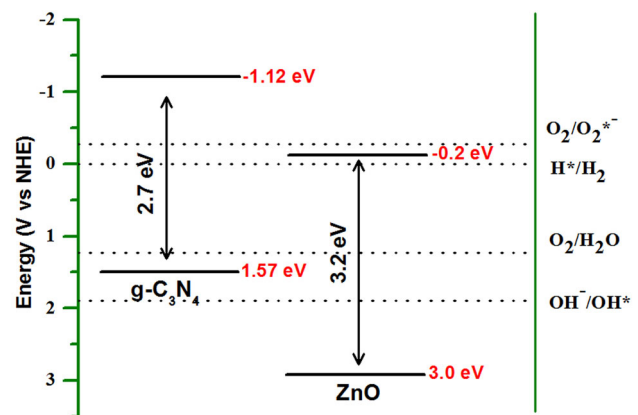
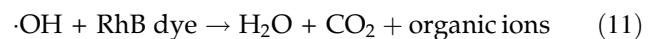
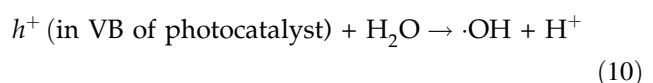
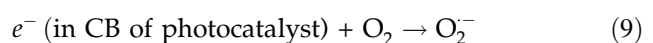


Fig. 11 Energy band structure of the prepared $g\text{-C}_3\text{N}_4@\text{ZnO}$ sample and mechanism for the photocatalytic dye degradation of RhB under visible light

When a photon with energy ($h\nu$) greater than the energy bandgap of materials strikes, electrons are moved from the valence band to the conduction band, leaving the valence band with an identical quantity of holes. Water molecules and dissolved oxygen in the water will now react with electrons and holes to produce $\cdot\text{OH}$ and $\text{O}_2^{\bullet-}$ radicals. These active species could quickly break down RhB dye into H_2O , CO_2 , and other organic ions in an aqueous solution according to reaction (8)–(12) [17–20, 36, 37].



Owing to the narrow bandgap, $g\text{-C}_3\text{N}_4@\text{ZnO}$ generates more photoexcited charge carriers and more reactive species. Also, designing $g\text{-C}_3\text{N}_4@\text{ZnO}$ hybrid nanostructure can prevent the recombination of charge carriers to some extent since photo-generated charge carriers from one semiconductor can end up in the conduction band or valence band of another due to an unsuitable band edge arrangement. Further, $g\text{-C}_3\text{N}_4$ can alter the exposed surface of ZnO crystal leads to enhanced surface active sites for photocatalytic reaction. The above factors may enhance the degradation of RhB dye into H_2O , CO_2 ,

and other organic ions than pure ZnO and g-C₃N₄ as per reaction (8)–(12). Hence g-C₃N₄@ZnO shows significantly high photocatalytic degradation efficiency against RhB dye than pristine ZnO and g-C₃N₄.

4 Conclusions

In this study, we have synthesized hexagonal cylinder-like twinned ZnO microcrystals by hydrothermal method and investigated the effect of g-C₃N₄ on its structural, optical, and photocatalytic characteristics. The addition of g-C₃N₄ not only affects the phase composition but also has a major impact on the growth of ZnO crystals by interacting with zinc precursor during the formation which leads to change in lattice parameter of the structure of ZnO and formation of g-C₃N₄@ZnO heterostructure (type II). Also, results showed that the typical hexagonal cylinder-like twinning ZnO microstructure could be transformed into a rice-like ZnO heterostructure by the addition of g-C₃N₄. The optical band gap was found to be 3.27 and 3.21 eV for pristine ZnO and g-C₃N₄-ZnO, respectively. The redshift toward the visible region in optical absorption and a significant reduction in the optical bandgap were observed for g-C₃N₄@ZnO heterostructure due to the narrow bandgap (~2.7 eV) of g-C₃N₄. Also, it was found that g-C₃N₄@ZnO degrades 92 % of RhB dye under 150 min of light irradiation and it is significantly higher than pristine ZnO (70 %). Designing g-C₃N₄@ZnO hybrid nanostructure can prevent the recombination of charge carriers which offered more number of •OH and O₂^{•-} radicals for the dye degradation leads to higher photocatalytic activity. This approach may be used to create efficient photocatalysts for environmental remediation in the near future.

Declarations

Conflict of interest The authors declare that they have no conflict of interest.

Supplementary Information: The online version contains supplementary material available at <http://doi.org/10.1007/s10854-021-06872-9>.

References

1. C.R. Holkar, A.J. Jadhav, D.V. Pinjari, N.M. Mahamuni, A.B. Pandit, A critical review on textile wastewater treatments: possible approaches. *J. Environ. Manag.* **182**, 351–366 (2016)
2. K.G. Pavithra, P.S. Kumar, V. Jaikumar, P.S. Rajan, Removal of colorants from wastewater: a review on sources and treatment strategies. *J. Ind. Eng. Chem.* **75**, 1–19 (2019)
3. N.Y. Donkadokula, A.K. Kola, I. Naz, D. Saroj, A review on advanced physico-chemical and biological textile dye wastewater treatment techniques. *Rev. Environ. Sci. Biotechnol.* **19**, 543–560 (2020)
4. R. Jain, M. Mathur, S. Sikarwar, A. Mittal, Removal of the hazardous dye rhodamine B through photocatalytic and adsorption treatments. *J. Environ. Manag.* **85**, 956–964 (2007)
5. M.S.S. Danish, L.L. Estrella, I.M.A. Alemaida, A. Lisin, N. Moiseev, M. Ahmadi, M. Nazari, M. Wali, H. Zaheb, T. Senjyu, Photocatalytic applications of metal oxides for sustainable environmental remediation. *Metals* **11**, 80 (2021)
6. C.W. Litton, D.C. Reynolds, T.C. Collins, *Zinc Oxide Materials for Electronic and Optoelectronic Device Applications* (Wiley, Hoboken, 2011)
7. C. Klingshirn, ZnO: material, physics and applications. *Chem. Phys. Chem.* **8**, 782–803 (2007)
8. A. Kołodziejczak-Radzimska, T. Jesionowski, Zinc oxide – from synthesis to application: a review. *Materials* **7**, 2833–2881 (2014)
9. N. Kamarulzaman, M.F. Kasim, R. Rusdi, Band gap narrowing and widening of ZnO nanostructures and doped materials. *Nanoscale Res. Lett.* **10**, 346 (2015)
10. C. Wang, Y. Gao, L. Wang, P. Li, Morphology regulation, structural, and photocatalytic properties of ZnO hierarchical microstructures synthesized by a simple hydrothermal method. *Phys. Status Solidi A* **214**, 1600876 (2017)
11. J. Duraimurugan, G.S. Kumar, M. Venkatesh, P. Maadeswaran, E.K. Girija, Morphology and size controlled synthesis of zinc oxide nanostructures and their optical properties. *J. Mater. Sci.: Mater. Electron.* **29**, 9339–9346 (2018)
12. W. Shi, S. Songa, H. Zhang, Hydrothermal synthetic strategies of inorganic semiconducting nanostructures. *Chem. Soc. Rev.* **42**, 5714–5743 (2013)
13. S. Liu, L. Zhu, W. Cao, P. Li, Z. Zhan, Z. Chen, X. Yuan, J. Wang, Defect-related optical properties of Mg-doped ZnO nanoparticles synthesized *via* low temperature hydrothermal method. *J. Alloys Compd.* **858**, 157654 (2021)
14. Y. Zhang, X. Yang, N. He, P. Zhang, Y. Ding, D. Liu, Z. Zou, J. Gui, One-step hydrothermal fabrication of erythrocyte-like ZnS/ZnO composite with superior visible light photocatalytic performance. *Mater. Lett.* **228**, 305–308 (2018)

15. M. Ismael, A review on graphitic carbon nitride (g-C₃N₄) based nanocomposites: synthesis, categories, and their application in photocatalysis. *J. Alloys Compd.* **846**, 156446 (2020)
16. B. Xu, M.B. Ahmed, J.L. Zhou, A. Altaee, G. Xu, M. Wu, Graphitic carbon nitride based nanocomposites for the photocatalysis of organic contaminants under visible irradiation: progress, limitations and future directions. *Sci. Total Environ.* **633**, 546–559 (2018)
17. S. Le, T. Jiang, Y. Li, Q. Zhao, Y. Li, W. Fang, M. Gong, Highly efficient visible-light-driven mesoporous graphitic carbon nitride/ZnO nanocomposite photocatalysts. *Appl. Catal.* **200**, 601–610 (2017)
18. P. Yang, J. Wang, G. Yue, R. Yang, P. Zhao, L. Yang, X. Zhao, D. Astruc, Constructing mesoporous g-C₃N₄/ZnO nanosheets catalyst for enhanced visible-light driven photocatalytic activity. *J. Photochem. Photobiol. A. Chem.* **388**, 112169 (2020)
19. M.A. Qamar, S. Shahid, M. Javed, S. Iqbal, M. Sher, A. Bahadur, M.M.A.L. Anazy, A. Laref, D. Li, Designing of highly active g-C₃N₄/Ni-ZnO photocatalyst nanocomposite for the disinfection and degradation of the organic dye under sunlight radiations. *Colloids Surf: A Physicochem. Eng. Asp.* **614**, 126176 (2021)
20. R. Manimozhi, M. Mathankumar, A.P.G. Prakash, Synthesis of g-C₃N₄/ZnO heterostructure photocatalyst for enhanced visible degradation of organic dye, *Optik* **229**, 165548 (2021).
21. J. Low, J. Yu, M. Jaroniec, S. Wageh, A.A. Al-Ghamdi, Heterojunction photocatalysts. *Adv. Mater.* **29**, 1601694 (2017)
22. M. Nishikawa, S. Yuto, T. Nakajima, T. Tsuchiya, N. Saito, Effect of lattice distortion on photocatalytic performance of TiO₂. *Catal. Lett.* **147**, 292–300 (2017)
23. S.N. Basahel, T.T. Ali, M. Mokhtar, Influence of crystal structure of nanosized ZrO₂ on photocatalytic degradation of methyl orange. *Nanoscale Res. Lett.* **10**, 73 (2015)
24. R. Boppella, K. Anjaneyulu, P. Basak, S.V. Manorama, Facile synthesis of face oriented ZnO crystals: tunable polar facets and shape induced enhanced photocatalytic performance. *Phys. Chem. C* **117**, 4597–4605 (2013)
25. D.F. Li, W.Q. Huang, L.R. Zou, G.F. Huang, Mesoporous g-C₃N₄ nanosheets: synthesis, superior adsorption capacity and photocatalytic activity. *J. Nanosci. Nanotechnol.* **18**, 5502–5510 (2018)
26. J. Duraimurugan, G.S. Kumar, P. Maadeswaran, S. Shanavas, P.M. Anbarasan, V. Vasudevan, Structural, optical and photocatalytic properties of zinc oxide nanoparticles obtained by simple plant extract mediated synthesis. *J. Mater. Sci.: Mater. Electron.* **30**, 1927–1935 (2019)
27. C. Suryanarayana, M.G. Norton, *X-Ray Diffraction A Practical Approach* (Springer, Boston, 1998)
28. Q. Zhong, H. Lan, M. Zhang, H. Zhu, M. Bu, Preparation of heterostructure g-C₃N₄/ZnO nanorods for high photocatalytic activity on different pollutants (MB, RhB, Cr(VI) and eosin). *Ceram. Inter.* **46**, 12192–12199 (2020)
29. D.J. Martin, K. Qiu, S.A. Shevlin, Highly efficient photocatalytic H₂ evolution from water using visible light and structure-controlled graphitic carbon nitride. *Angew. Chem. Int. Ed.* **53**, 9240–9245 (2014)
30. J.F. Moulder, *Handbook of X-Ray Photoelectron Spectroscopy: A Reference Book of Standard Spectra for Identification and Interpretation of XPS Data* (Perkin-Elmer Corporation, Eden Prairie, 1992)
31. Y. Yang, J. Chen, Z. Mao, N. An, D. Wang, B.D. Fahlman, Ultrathin g-C₃N₄ nanosheets with an extended visible-light-responsive range for significant enhancement of photocatalysis. *RSC Adv.* **7**, 2333–2341 (2017)
32. T. Prakash, G. Neri, A. Bonavita, E. Ranjith Kumar, K. Gnanamoorthi, Structural, morphological and optical properties of Bi-doped ZnO nanoparticles synthesized by a microwave irradiation method. *J. Mater. Sci.: Mater. Electron.* **26**, 4913–4921 (2015)
33. Y. Köseoğlu, A simple microwave-assisted combustion synthesis and structural, optical and magnetic characterization of ZnO nanoplatelets. *Ceram. Int.* **40**, 4673–4679 (2014)
34. A. Manikandan, E. Manikandan, B. Meenatchi, S. Vadivel, S.K. Jaganathan, R. Ladhumanandasivam, M. Henini, M. Maaza, J.S. Aananda, Rare earth element (REE) lanthanum doped zinc oxide (La: ZnO) nanomaterials: synthesis structural optical and antibacterial studies. *J. Alloys Compd.* **723**, 1155–1161 (2017)
35. M. Ismael, The photocatalytic performance of the ZnO/g-C₃N₄ composite photocatalyst, toward degradation of organic pollutants and its inactivity toward hydrogen evolution: The influence of light irradiation and charge transfer. *Chem. Phys. Lett.* **739**, 136992 (2020)
36. C.B. Ong, L.Y. Ng, A.W. Mohamm, A review of ZnO nanoparticles as solar photocatalysts: synthesis, mechanisms and applications. *Renew. Sustain. Energy Rev.* **81**, 536–551 (2018)
37. K.M. Lee, C.W. Lai, K.S. Ngai, J.C. Juan, Recent developments of zinc oxide based photocatalyst in water treatment technology: a review. *Water Res.* **88**, 428–448 (2016)

Publisher's Note Springer Nature remains neutral with regard to jurisdictional claims in published maps and institutional affiliations.